Supporting Information

Sulfur-doped g-C_3N_4/V_2C MXene Schottky junctions for superior photocatalytic H_2 evolution

Haitao Wang[a], Jipeng Fan[a], Jing Zou[a], Yujie Zheng[b], Dingsheng Wang[c], Jizhou Jiang[a,*]

[a]*School of Chemistry and Environmental Engineering, School of Environmental Ecology and Biological Engineering, Key Laboratory of Green Chemical Engineering Process of Ministry of Education, Engineering Research Center of Phosphorus Resources Development and Utilization of Ministry of Education, Novel Catalytic Materials of Hubei Engineering Research Center, Wuhan Institute of Technology, Wuhan 430205, P. R. China.*

[b]*MOE Key Laboratory of Low-grade Energy Utilization Technologies and Systems, CQU-NUS Renewable Energy Materials & Devices Joint Laboratory, School of Energy & Power Engineering, Chongqing University, Chongqing 400044, P. R. China.*

[c]*Department of Chemistry, Tsinghua University, Beijing 100084, P. R. China.*

Corresponding Email: 027wit@163.com

Experimental section

Chemicals and materials

V_2AlC (98%) Lithium fluoride (LiF, 98%) was bought from Shanghai Macklin Reagent. Hydrofluoric acid (HF, ≥40%), triethanolamine (TEOA), melamine (≥99.5%), and sodium sulfate anhydrous (Na_2SO_4, 99%) were purchased from Aladdin Chemicals Reagent Technology Co., Ltd. Hydrochloric acid (HCl) was provided by Sinopharm. All the chemicals were analytical reagents and used directly without further purification.

Synthesis of V_2C

The V_2AlC MAX phase precursor etching was used to obtain multilayer V_2C. 0.5 g of V_2AlC was added to a teflon-lined reactor equipped with 1 g of LiF and 20 ml (9 mol) HCl etch agent and etched at 90 °C for 72 h. The obtained suspension was centrifuged at 3500 rpm for 10 minutes, washed thoroughly with deionized water until the pH value reached 7, and then dried at 60 °C in a vacuum oven. Multilayer V_2C precipitates were obtained.

Preparation of SCN

Melamine (10 g) was placed in a porcelain boat and calcined at 520 °C in the air at a heating rate of 10 °C min^{-1} for 4 h to obtain light yellow CN. 0.35 g CN and 2.45 g sulfur powder were added to the ball mill tank, and then the ball mill tank was pumped to vacuum by a circulating water vacuum pump. After grinding for 10 min, the samples were collected, and the mixture of sulfur powder and CN were transferred to the porcelain boat. SCN was obtained by calcining the mixture at 530 °C for 3 h in a tube furnace (5 °C min^{-1}) in an N_2 atmosphere.

Fabrication of SCN/V_2C heterojunction

2.45 g sulfur powder, 0.35 g CN, and 5 mg V_2C were added to the ball mill tank, and then the ball mill tank was pumped to vacuum by circulating water vacuum pump. The samples were collected after grinding

for 10 min, and the mixture of sulfur, CN, and V_2C was transferred to the porcelain boat. SCN/V_2C composites were obtained by calcining the mixture at 5 °C min^{-1} at 530 °C for 3 h in a tube furnace in N_2 atmosphere.

Physical characterizations

A field emission scanning electron microscopy (FESEM, Gemini SEM 300, Germany Zeiss) with an energy-dispersive X-ray spectroscope (EDX) was employed to examine the surface morphology and element composition of as-obtained catalysts. The microstructure of all samples was examined by transmission electron microscopy (TEM) using a Tecnai G2 20 microscope operating at an acceleration voltage of 200 kV. A powder X-ray diffractometer (XRD, Bruker D8 ADVANCE diffractometer) was used to record the crystallographic structures of all samples. An X-ray photoelectron spectroscopy (XPS, ESCALAB XI^+ -600W, Thermo Fisher Scientific) was adopted to analyze the electronic structures and surface chemical components of as-obtained photocatalysts. The surface area (BET) and pore size distributions (PSD) were recorded by N_2 adsorption-desorption isotherm on a surface analyzer (ASAP 2020 HD88, Micromeritics USA). The pore size distributions were calculated according to the Barrett-Joyner-Halenda (BJH) method from the branch of adsorption isotherm.

Photoelectrochemical measurements

UV-Vis diffuse reflectance spectra were measured by a Carry5000 UV-vis spectrophotometer (Agilent). FT-IR spectra were obtained on a Thermo Nicolet Avatar 6700 FTIR spectrophotometer (Thermo Fisher Scientific). A contact angle measuring device (OCA 20, Dataphysics, Germany) was employed to study the wetting properties of the membranes. Transient fluorescence decay (TFD) Spectra and photoluminescence (PL) emission spectra of as-obtained photocatalysts were performed by an Edinburgh-FLS980 (England) spectrophotometer.

The wettability of the liquid medium on the surface of the sample was tested by a contact angle measuring device (OCA 20, Dataphysics, Germany). A total of 50 mg of the photocatalytic sample was pressed to 10 MPa using a tablet press (YP-12). The prepared flakes were attached to the glass slides and loaded on the lifting platform of the contact angle tester, and the deionized water was used as the liquid medium for testing.

Transient photocurrent (TPC) responses and electrochemical impedance spectroscopy (EIS) measurements were evaluated on an electrochemical workstation (CHI660e Instruments) with a standard three-electrode photoelectrochemical cell, where an Ag/AgCl electrode, a platinum-wire electrode and a photocatalyst-coated glassy carbon electrode (GCE, 3 mm in diameter) were employed as the reference, counter, and working electrodes, respectively. Moreover, the recorded potential was converted to a reversible hydrogen electrode (RHE) by the following equation: $E_{RHE}=E_{Ag/AgCl} + 0.1987 + 0.05916 \bullet pH$. For working electrode preparation, 10 mg of as-prepared photocatalysts were mixed with 5 mL of deionized water, and then 5 μL of the homogeneous suspension was pipetted onto a photocatalyst-coated GCE (3 mm in diameter). The electrolytes required for TPC responses and EIS tests were 0.5 M Na_2SO_4 (pH = 6.7) and 5 mmol L^{-1} potassium ferricyanide solution, respectively. In addition, a 10 W xenon lamp (410~420 nm) was employed as the light source during the TPC response measurement.

Photocatalytic hydrogen evolution tests

The photocatalytic hydrogen evolution measurements were carried out in a full glass automatic online four-trace gas analysis system (Labsolar-6A, Beijing PerfectLight, China). A Xe lamp with an output power of 300 W (with a $\lambda \geq 420$ nm cutoff filter as simulated visible light) acted as the light source.

In a typical process, 10 mL of triethanolamine (TEOA, sacrificial electron donors) and 20 mg of photocatalysts were added into 90 mL of deionized water. Then, 3 wt% of platinum provided by $H_2PtCl_6 \cdot 6H_2O$ was added to the mixed solution as a co-catalyst. Necessarily, the above photocatalyst solution was sonicated for at least 30 min before light exposure. Moreover, the photoreactor was also evacuated for 10 min until air was completely removed before testing.

During photocatalytic tests, the suspension was stirred continually, and the gas concentration balance was flowed by a fan. Additionally, the circulating cooling water (10 ℃) system was kept open throughout the whole photocatalytic HER process to eliminate the thermal effect of photocatalysts. The generated H_2 by photocatalytic HER was detected by an online gas chromatograph accompanied by a thermal conductivity detector (GC9790II, China) with Argon as carrier gas. The amount of generated H_2 was estimated from the corresponding calibration plot. The apparent quantum efficiency (AQE) was measured according to the following equations.

$$\mathrm{AQE}(\%) = \frac{\text{number of reacted electrons}}{\text{number of incident photons}} \times 100\%$$

$$= \frac{2 \times \text{number of evolved } H_2 \text{ molecules}}{\text{number of incident photons}} \times 100\%$$

Details of theoretical calculations

The first principles density functional theory (DFT) calculation module CASTEP in Materials Studio software were used for geometry optimization and charge density difference calculation. The Broyden-Fletcher-Goldfarb-Shanno (BFGS) algorithm and the generalized gradient approximation (GGA) of the PBE scheme were employed to calculate the developed catalysts. The cut-off energy was 520 eV. The Brillouin zone was sampled with a 2 × 2 × 1 k-point grid based on the Monk horstPack method and the semiempirical dispersion correction of the Grimme scheme was considered for geometric optimization of all photocatalysts. The total energy of the convergence criterion for geometric optimization was 1.0×10^{-5} eV·atom^{-1}. The maximum force was 0.03 eV·Å^{-1} (1 Å = 0.1 nm), the maximum stress and maximum displacement were 0.05 GPa and 1.0×10^{-3} Å, respectively.

The work functions of as-obtained catalysts were also calculated, which were dependent on the position of the Fermi level. The orbitals of developed photocatalysts were calculated through the DMol3 module of Materials Studio software. In generalized gradient approximation, the exchange-correlation function in the form of Perdew-Burke-Ernzerhof was used to calculate the catalyst surfaces. The cut-off energy was 400 eV. The Brillouin zone was sampled with a 3 × 3 × 1 k-point grid based on the Monk horstPack method and the semiempirical dispersion correction of the Grimme scheme was considered for geometric optimization of all samples. The total energy of the convergence criterion for geometric optimization was 1.0×10^{-5} Ha. The maximum force was 0.002 Ha·Å^{-1} (1 Å = 0.1 nm), the maximum displacementwas 5.0×10^{-3} Å.

The free energy calculation of hydrogen adsorption (ΔG_{H*}) was based on Nørskovetals' calculation hydrogen electrode (CHE) model, which was defined as follows:

$$\Delta G_{H*} = \Delta E_{H*} + \Delta ZPE - T\Delta S$$

Where ΔE, ΔZPE, and ΔS respectively represented the changes in electronic energy, zero-point energy, and entropy that were caused by the adsorption of hydrogen. The ideal hydrogen adsorption free energy value (ΔG_{H*}) was near zero, which could balance the adsorption and desorption of hydrogen reactions.

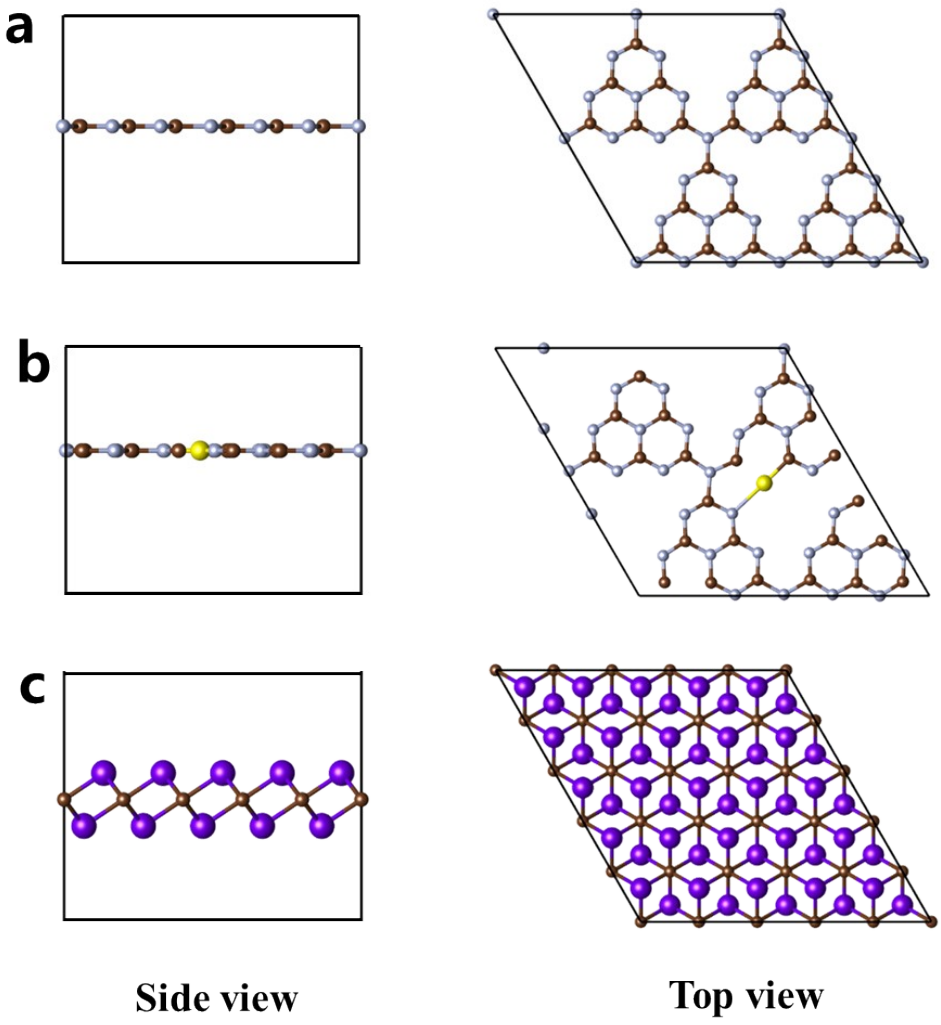

Figure S1. Theoretical structural model of (a) CN, (b) SCN, and (a) V_2C.

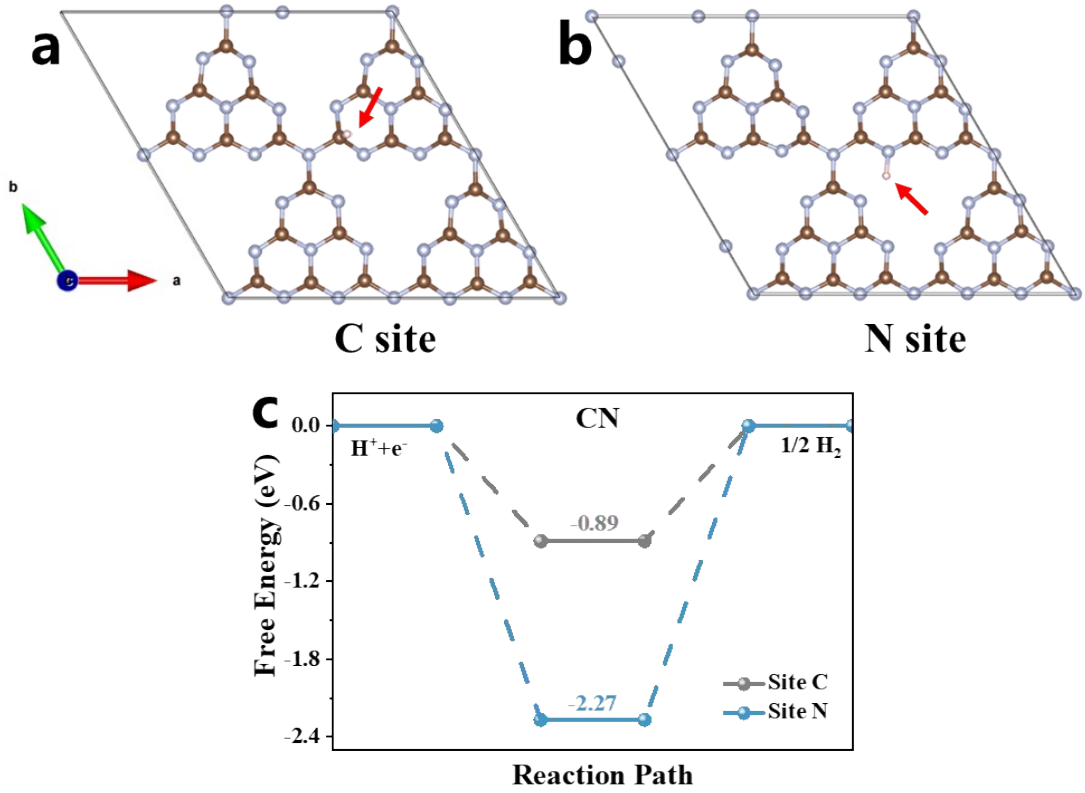

Figure S2 (a-b) Optimized structures and (c) Gibbs free energy changes of H* intermediates in C and N sites for CN.

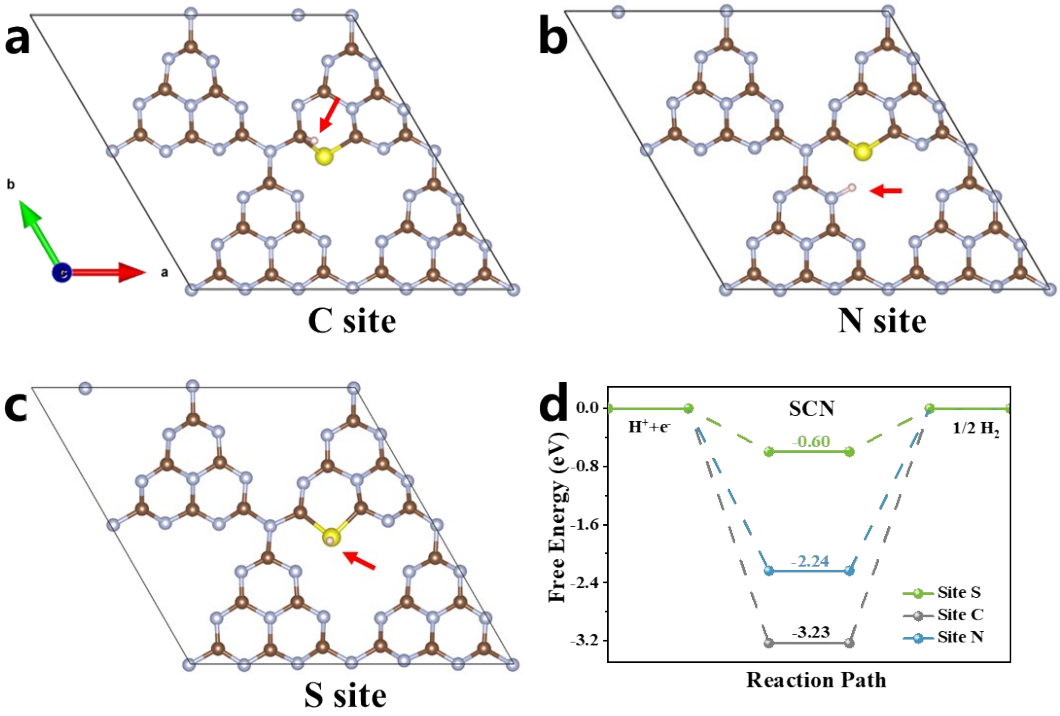

Figure S3. (a-c) Optimized structures and (d) Gibbs free energy changes of H* intermediates in C, N, and S sites for SCN.

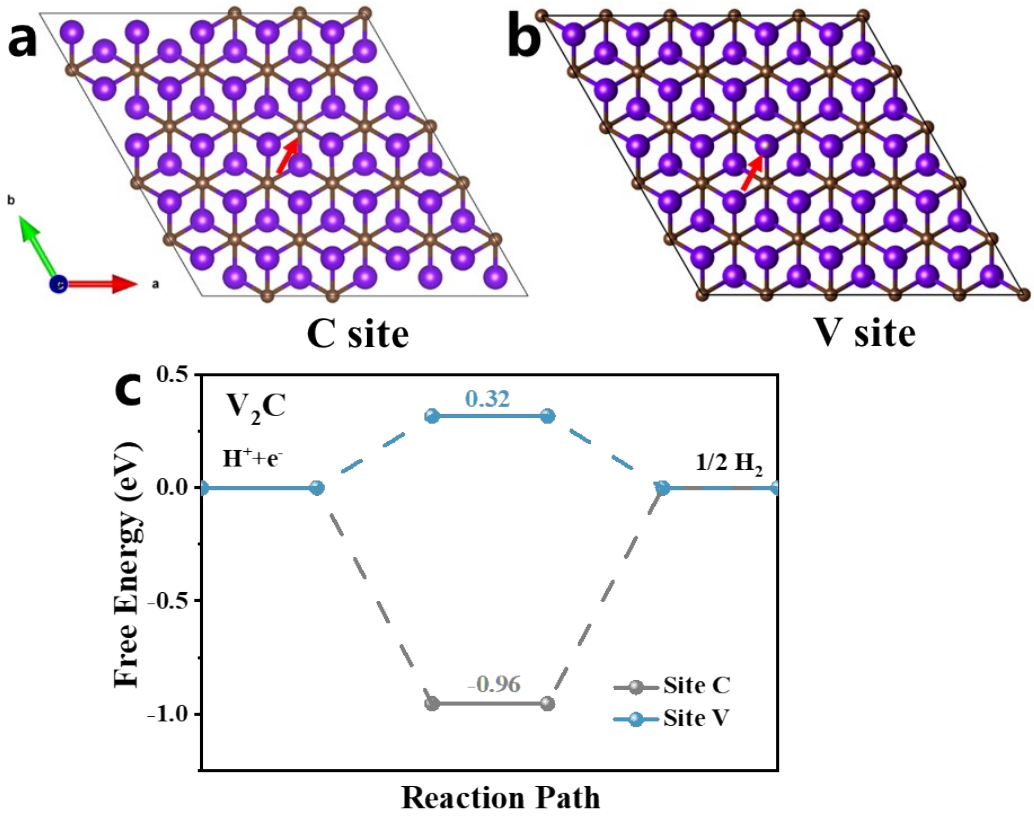

Figure S4. (a-b) Optimized structures and (c) Gibbs free energy changes of H* intermediates in C and V sites for V_2C.

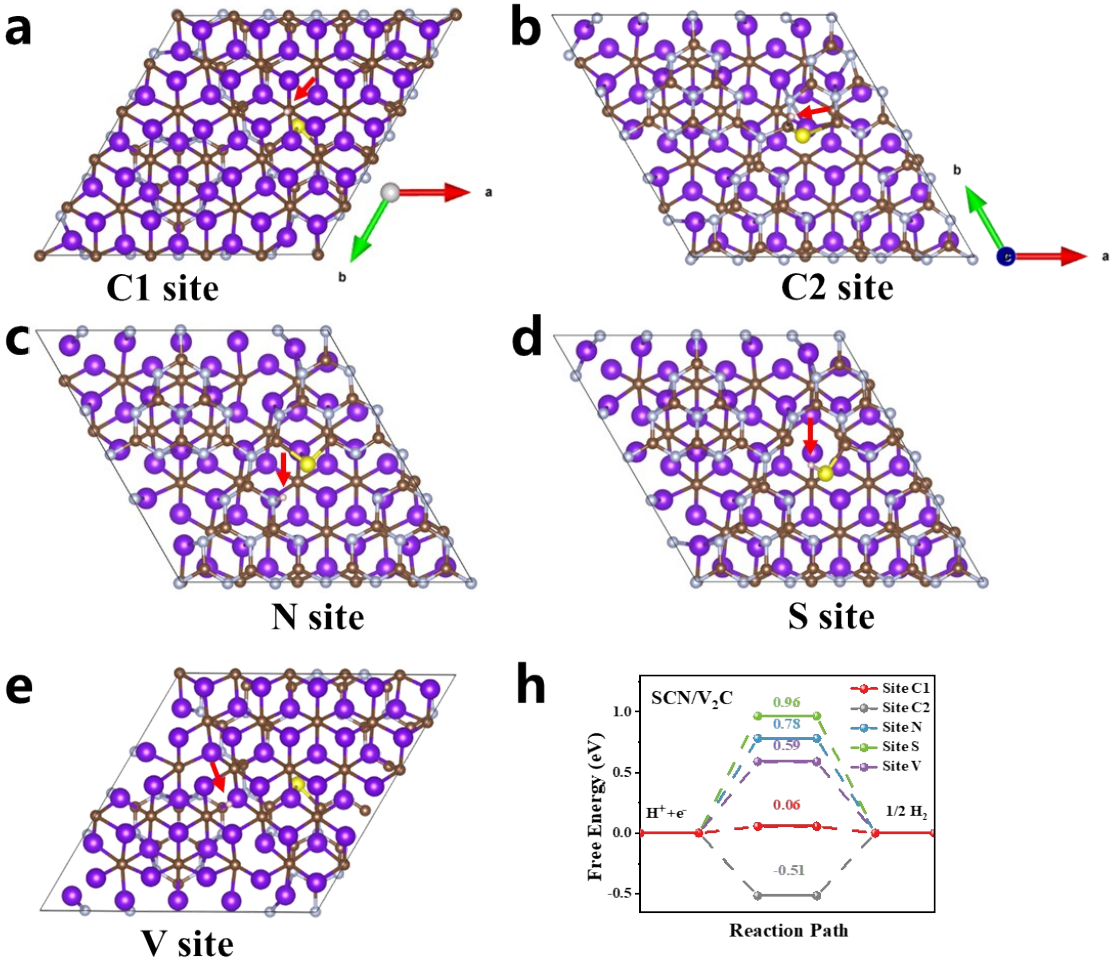

Figure S5. (a-e) Optimized structures and (h) Gibbs free energy changes of H* intermediates in C1, C2, N, S, and V sites for SCN/V_2C heterojunction.

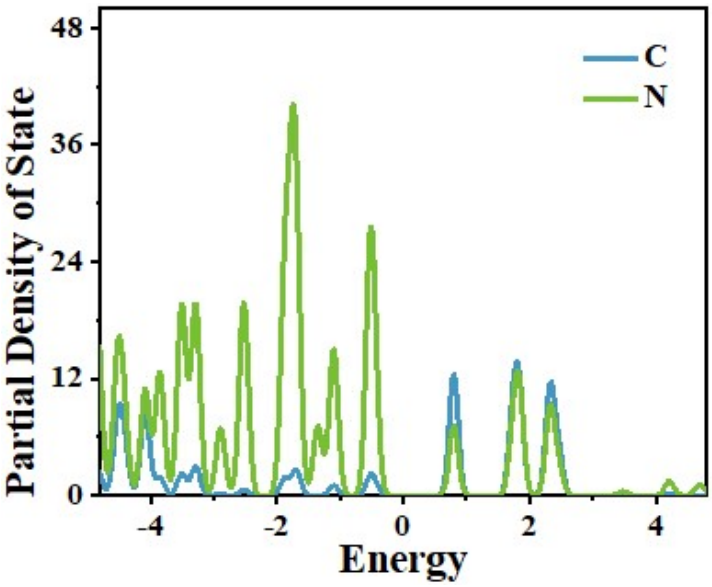

Figure S6. Partial density of states for CN.

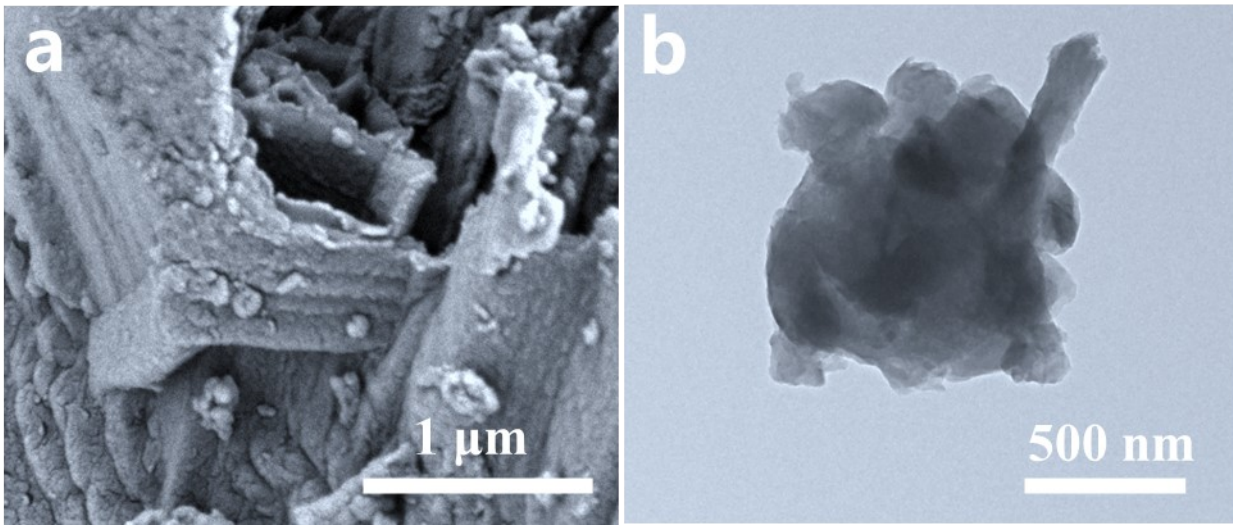

Figure S7. (a-b) SEM and TEM images of CN.

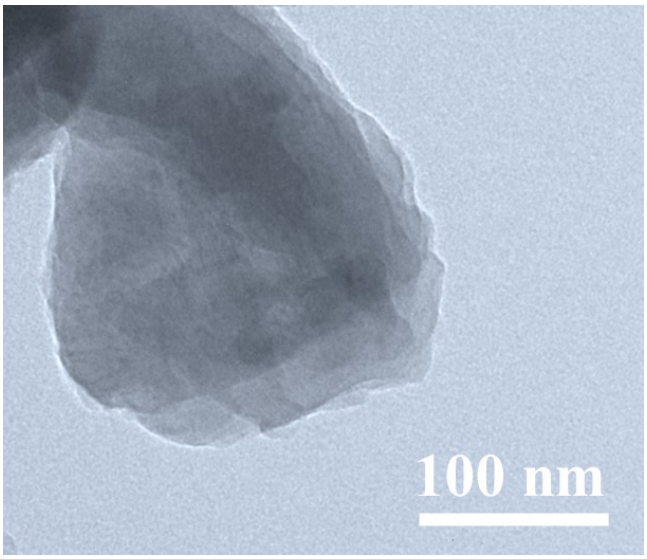

Figure S8. (a-b) TEM images of SCN.

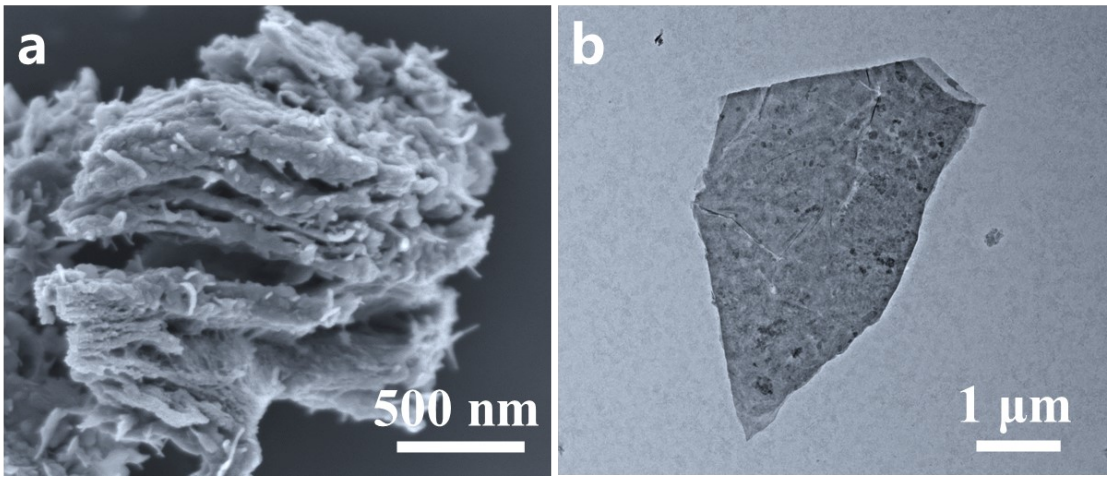

Figure S9. (a-b) SEM and TEM images of V_2C.

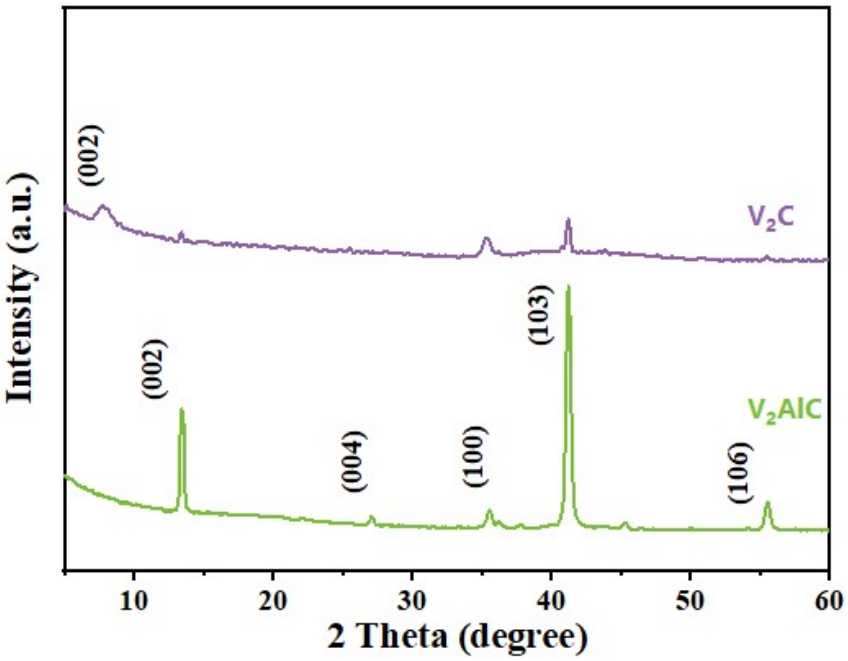

Figure S10. XRD patterns of V_2C, V_2AlC.

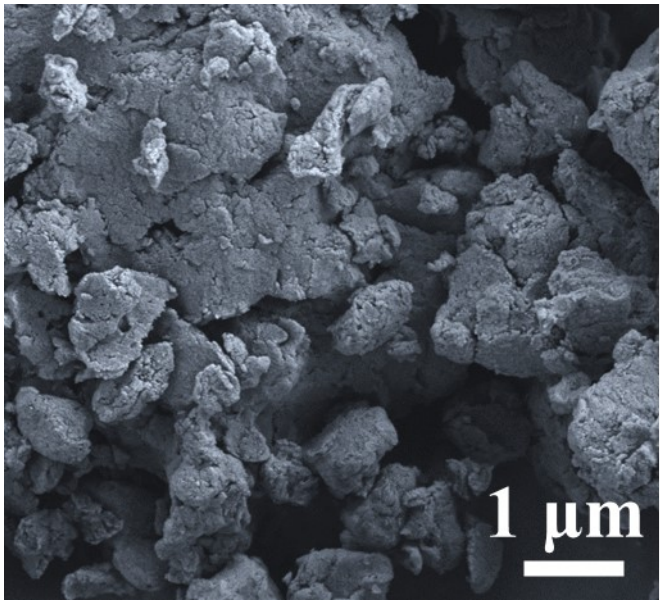

Figure S11. SEM images of SCN/V_2C heterojunction.

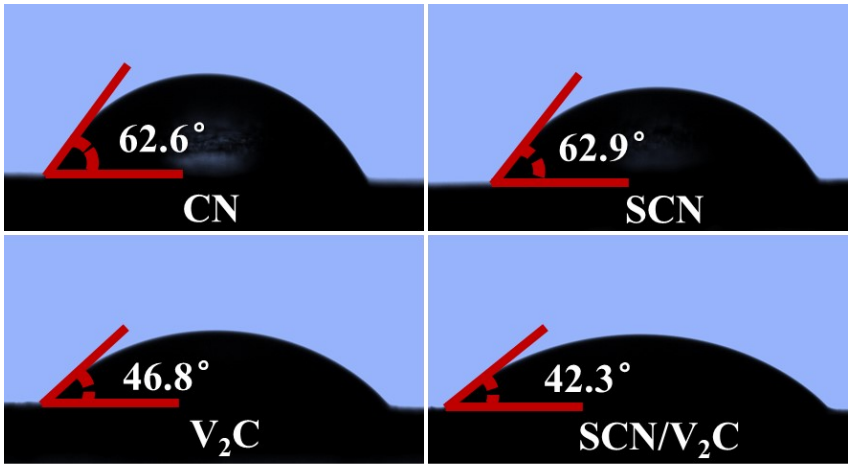

Figure S 12. The contact Angle of CN, SCN, V_2C, SCN/V_2C.

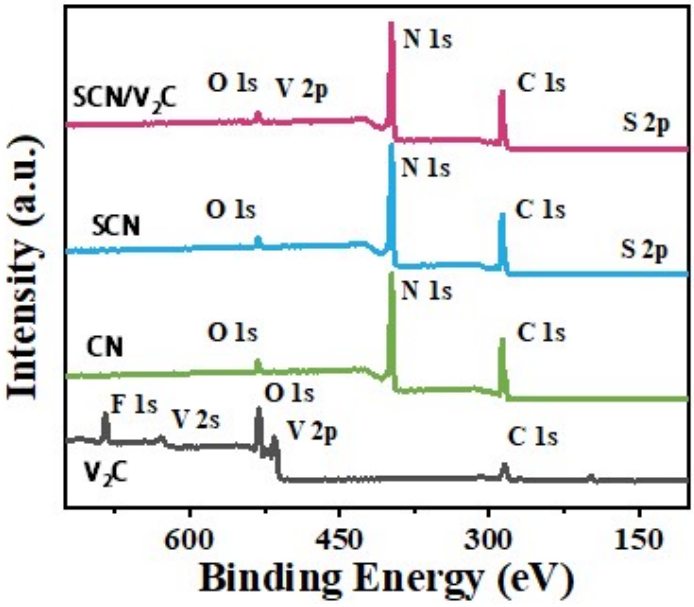

Figure S13. The high-resolution XPS survey spectra of V_2C, CN, SCN, SCN/V_2C.

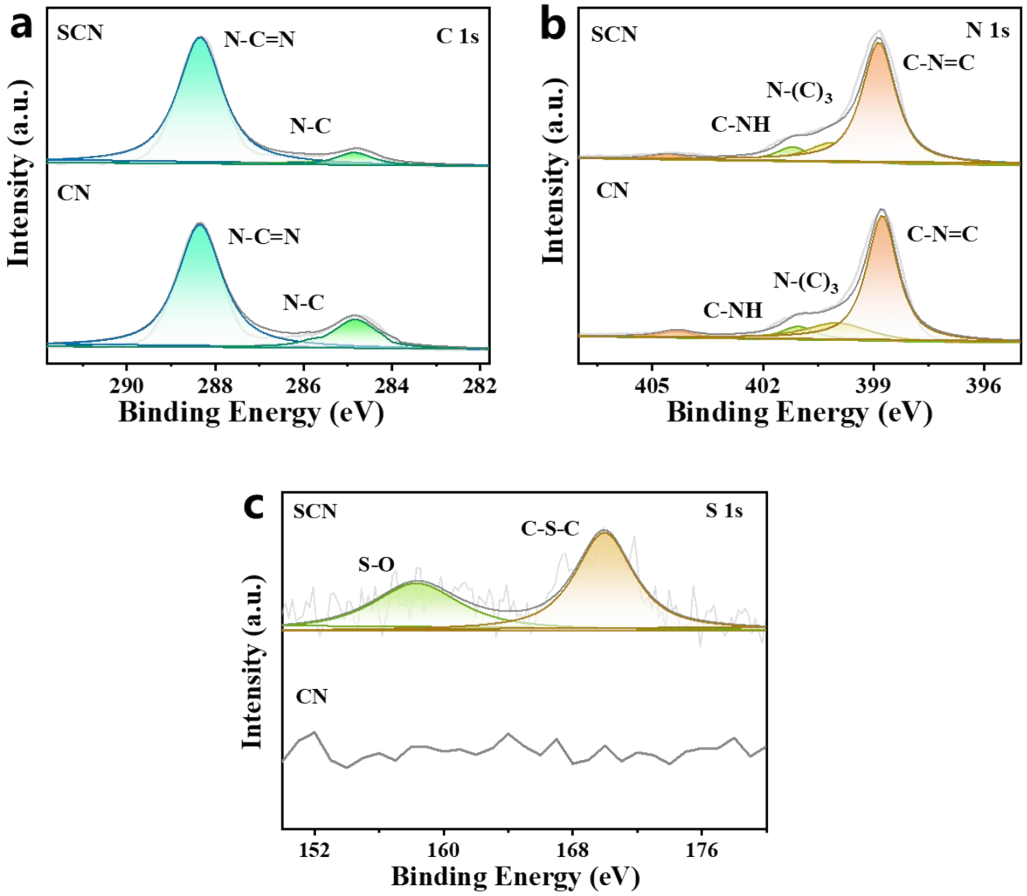

Figure S14. (a-c) The high-resolution XPS spectra of C 1s, N 1s, and S 1s of CN.

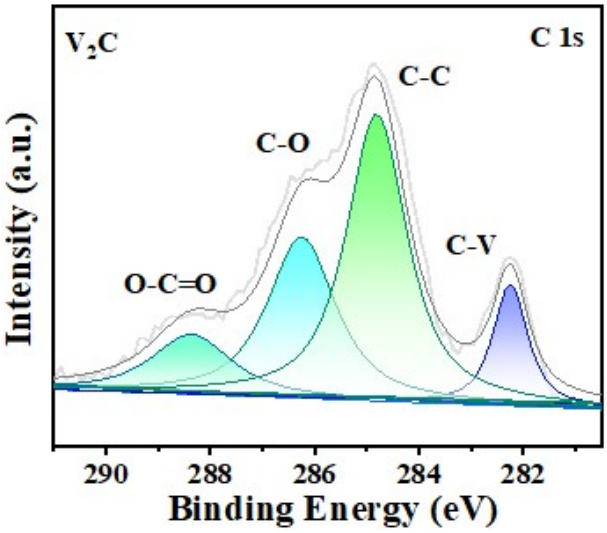

Figure S15. The high-resolution XPS spectra of C 1s of V_2C.

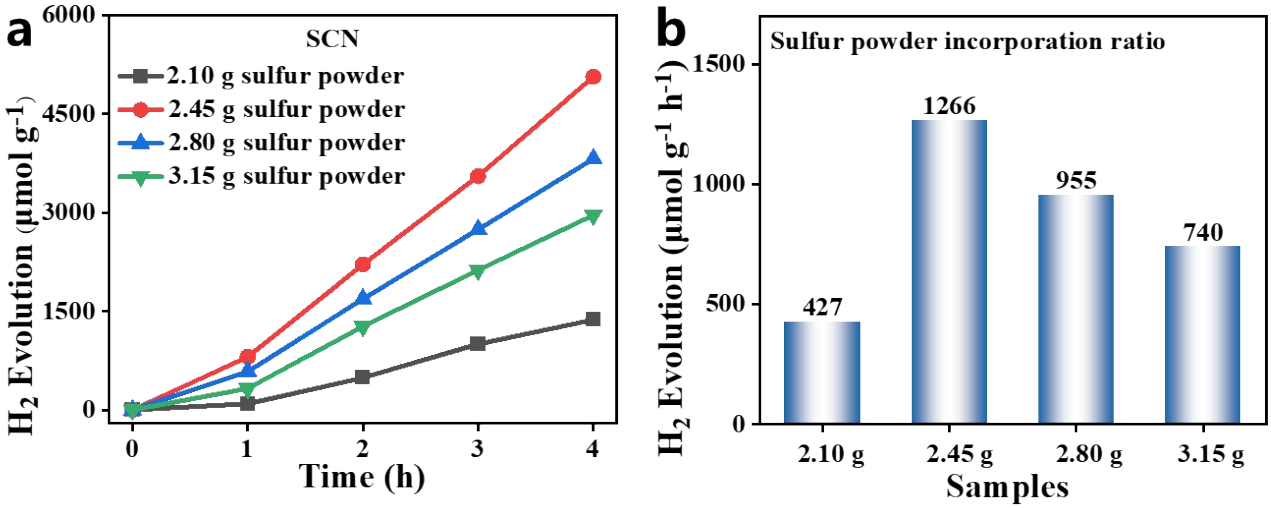

Figure S16. (a-b) Photocatalytic H_2 evolution activities of SCN obtained at different sulfur powder contents.

225

226

227

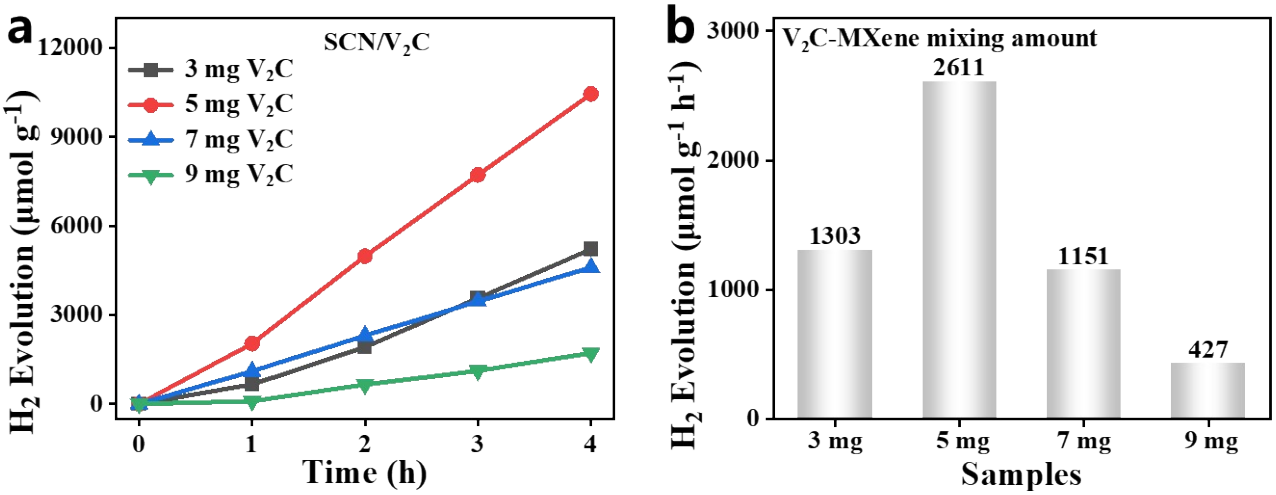

228

229 **Figure S17.** (a-b) Photocatalytic H_2 evolution activities of SCN/V_2C obtained at different V_2C MXene
230 contents.

231

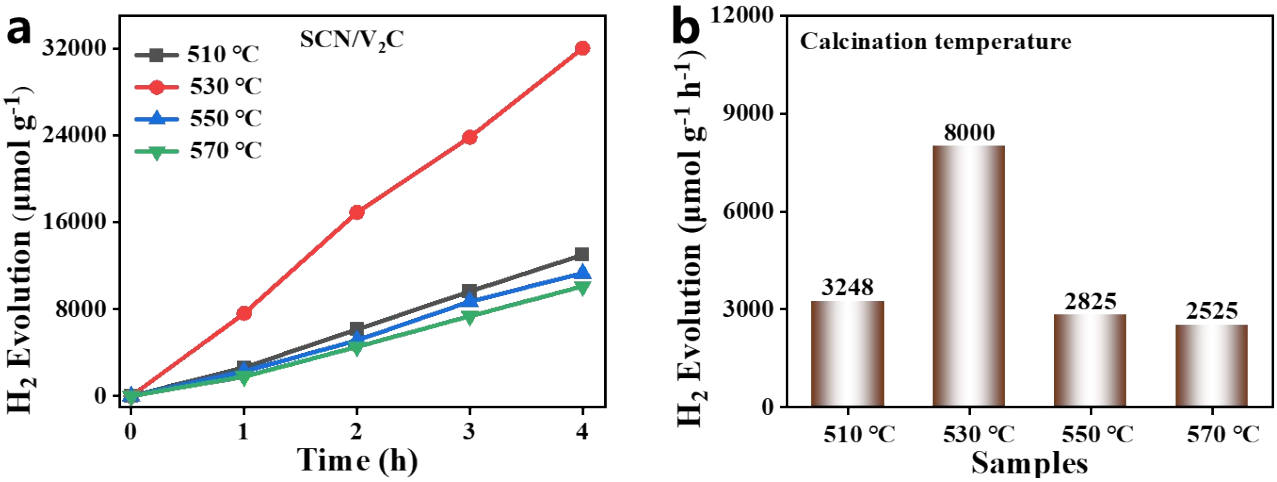

Figure S18. (a-b) Photocatalytic H_2 evolution activities of SCN/V_2C were obtained at different calcination temperatures.

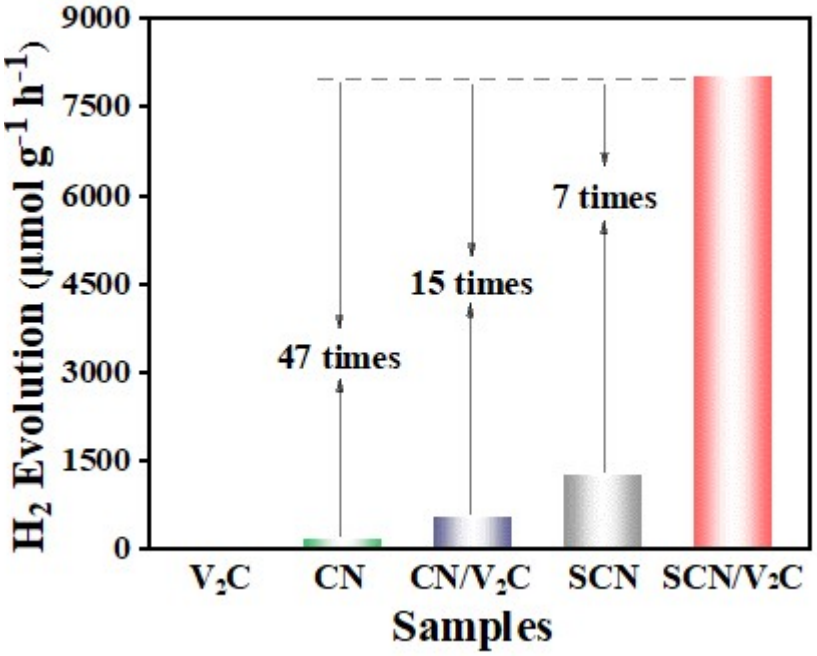

Figure S19. The enhanced photocatalytic H_2 production rate of SCN/V_2C was compared with V_2C, CN, SCN, and CN/V_2C.

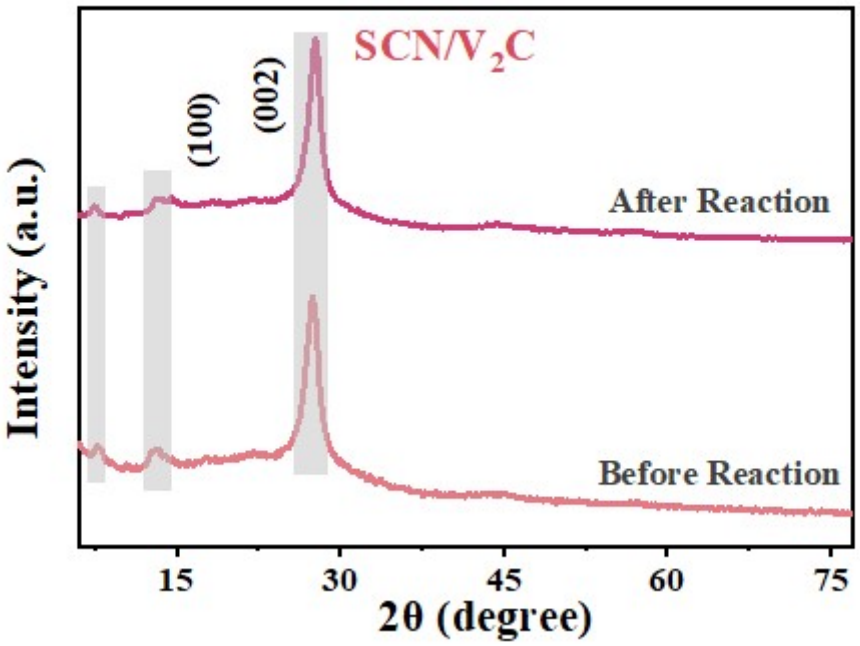

Figure S20. XRD patterns of SCN/V_2C before and after cycle reaction.

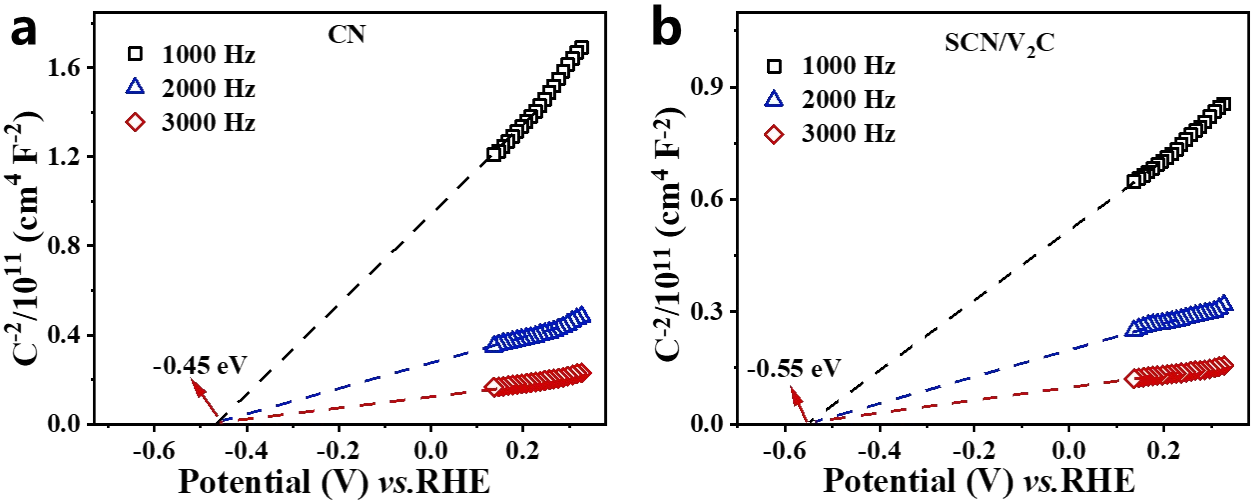

Figure S21. (a-b) M-S plots of CN, SCN/V_2C at different frequencies.

The slope of the M-S curve is positive, indicating that the material is an n-type semiconductor, and the E_{CB} of the n-type semiconductor is more negative than the corresponding E_{fb} (flat band potential) (about 0.3 V).

E_{CB} (RHE) = E_{fb} - 0.3

E_{CB} (vacuum level) = E_{CB} (RHE) - 4.5

In addition, the corresponding E_{VB} values can be obtained according to Eg and conduction band potential (E_{CB}) values.

E_{CB} (RHE) = E_{VB} (RHE) - Eg

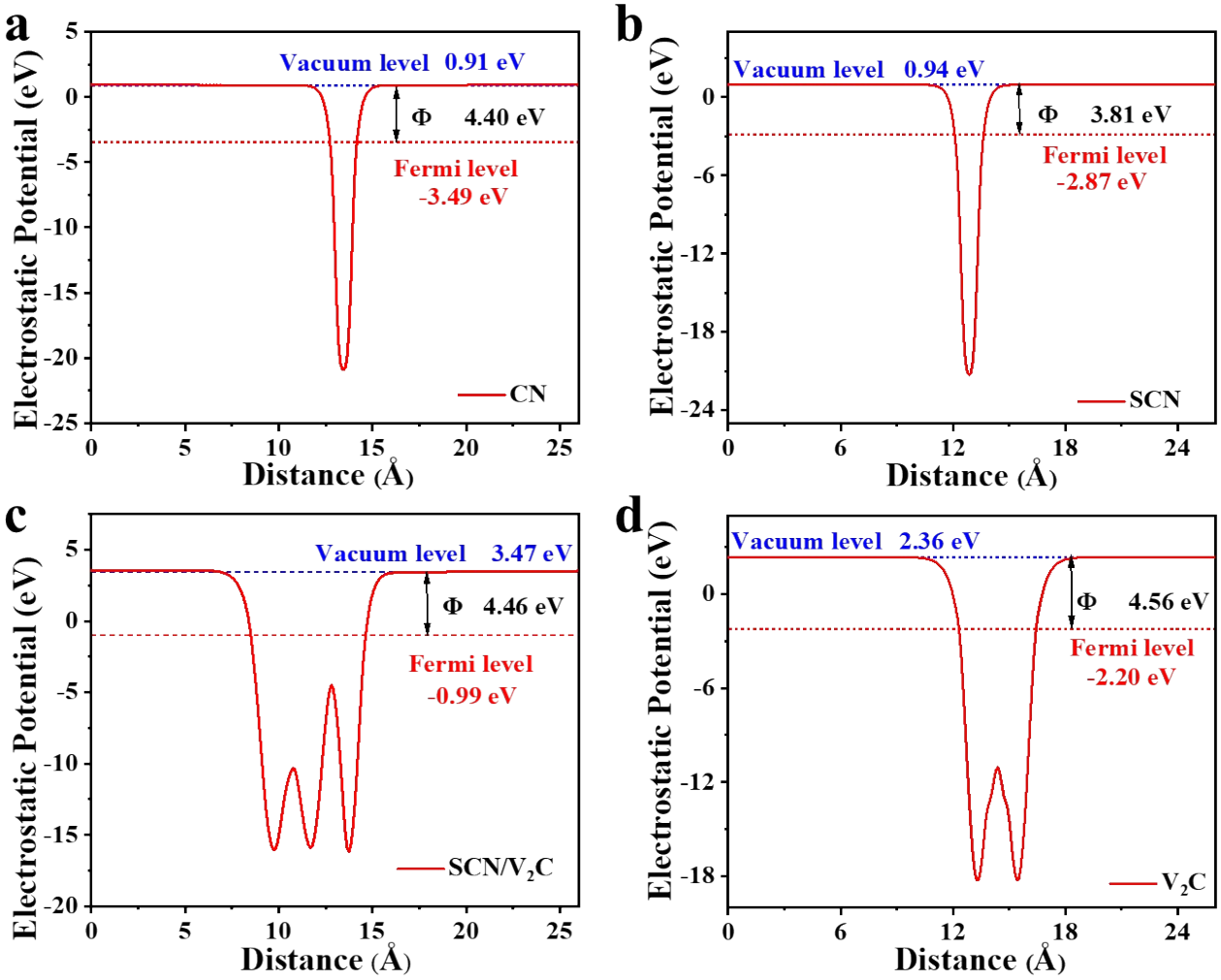

Figure S22. The calculated work functions of (a) CN, (b) SCN, (c)V_2C and (d)SCN/V_2C heterojunction.

The electron work function (Φ) is defined as the difference between the vacuum energy level (E_V) and the Fermi energy level (E_F). $\Phi = E_V - E_F$

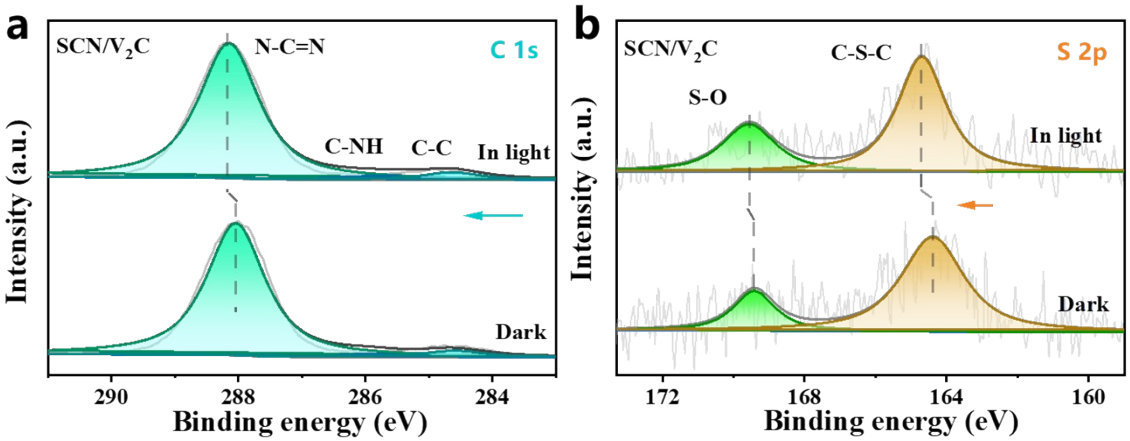

Figure S23. *In situ* irradiated spectra of (a) C 1s and (b) S 2p for SCN/V_2C heterojunction.

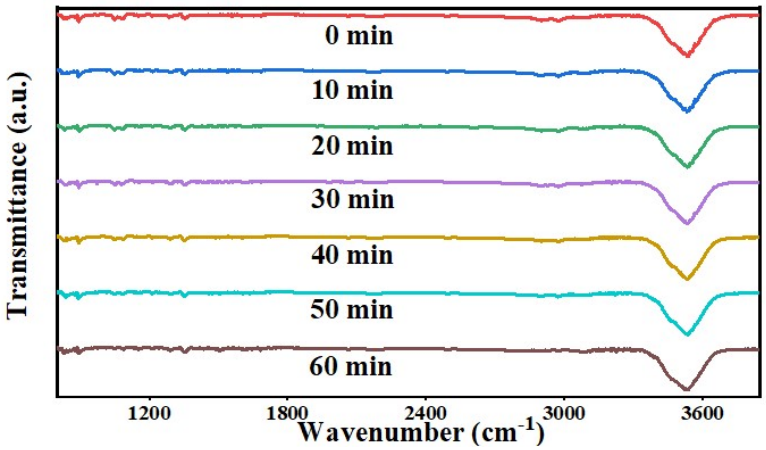

Figure S24. *In situ* Fourier infrared spectra of SCN/V_2C heterojunction.

Table S1 elements contents of V_2C, CN, SCN, SCN/V_2C heterojunction derived from XPS (at %).

Sample	C (at %)	N (at %)	S (at %)	V (at %)
V_2C	70.24	/	/	29.76
CN	47.56	52.44	/	/
SCN	44.35	55.35	0.3	/
SCN/V_2C	43.83	55.51	0.28	0.38

Table S2 The XPS results of C 1s and V 2p for V_2C.

Peak	Binding energy (eV)	Assignment	FWHM (eV)	Peak area
C 1s	288.3	O-C=O	1.8	4716.10
	286.2	C-O	1.6	10822.17
	282.2	C-V	0.8	4173.22
V 2p	524.5	V^{4+}	2	1693.67
	522.7	V^{3+}	1.8	458.70
	521.5	V^{2+}	1.9	893.57
	517.1	V^{4+}	1.9	2343.71
	515.5	V^{3+}	1.6	234.51
	514.1	V^{2+}	1.5	488.67

299

300

301

302 **Table S3** The XPS results of C 1s and N 1s for CN.

Peak	Binding energy (eV)	Assignment	FWHM (eV)	Peak area
C 1s	288.3	N-C=N	1.2	94733.39
	286.6	C-N	2	3974.90
N 1s	401.1	C-NH	1.1	13134.88
	400.1	$N-(C)_3$	2	35082.46
	398.9	C-N=C	1.1	134716.7

303

304

Table S4 The XPS results of C 1s, N 1s, and S 2p for SCN.

Peak	Binding energy (eV)	Assignment	FWHM (eV)	Peak area
C 1s	288.3	N-C=N	1.2	97508.77
	286.3	N-C	2	4573.74
N 1s	401.0	C-NH	1.5	14295.44
	400.0	$N-(C)_3$	1.6	29407.77
	398.6	C-N=C	1.2	142522.3
S 2p	170.1	S-O	2	135.49
	164.7	C-S-C	2.5	913.07

311

312

313

314 **Table S5** The XPS results of C 1s, N 1s, S 2p, and V 2p for SCN/V_2C heterojunction.

Peak	Binding energy (eV)	Assignment	FWHM (eV)	Peak area
C 1s	288.5	N-C=N	1.3	95194.59
	286.7	N-C	1.5	3041.72
N 1s	401.1	C-NH	1.0	20603.64
	400.1	$N-(C)_3$	1.5	27735.66
	398.8	C-N=C	1.1	150501
S 2p	170.3	S-O	3	557.03
	165.1	C-S-C	2	768.84
V 2p	524.3	V^{4+}	2.14	16479.81
	522.4	V^{3+}	1.54	7118.41
	520.6	V^{2+}	1.14	8283.49
	516.4	V^{4+}	2	50331.63
	514.4	V^{3+}	2	19389.83
	513.7	V^{2+}	1.5	27933.22

315

316

Table S6 Photocatalytic H_2 precipitation activity and comparison of catalyst variables.

Catalyst	catalyst quantity (mg)	Light Source	Reaction condition	Co-catalyst	H_2 ($\mu mol\ g^{-1}\ h^{-1}$)
SCN/V_2C	**20**	**300 W Xemon**	**Water (90 mL) TEOA (10 mL)**	**Pt (3 wt.%)**	**8003**
V_2C	**20**	**300 W Xemon**	**Water (90 mL) TEOA (10 mL)**	**Pt (3 wt.%)**	**4**
CN	**20**	**300 W Xemon**	**Water (90 mL) TEOA (10 mL)**	**Pt (3 wt.%)**	**175**
CN/V_2C	**20**	**300 W Xemon**	**Water (90 mL) TEOA (10 mL)**	**Pt (3 wt.%)**	**539**
SCN	**20**	**300 W Xemon**	**Water (90 mL) TEOA (10 mL)**	**Pt (3 wt.%)**	**1266**

Table S7 The comparisons of photocatalytic H_2 evolution activities between SCN/V_2C heterojunction and other MXenes or g-C_3N_4 based photocatalysts previously reported.

Catalyst	Light Source	Reaction condition	Co-catalyst	H_2 (μmol $g^{-1}h^{-1}$)	Ref.
SCN/V_2C	300 W Xemon	Water (90 mL) TEOA (10 mL)	Pt (3 wt.%)	8003	This work
g-C_3N_4/WO_3	350 W Xemon	Water (85 mL) TEOA (15 mL)	Pt (3 wt.%)	482	1
$ZnIn_2S_4$/$Ti_3C_2T_x$	300 W Xemon	Water (90 mL) TEOA (10 mL)	Pt (3 wt.%)	3475	2
$ZnIn_2S_4$/g-C_3N_4/Ti_3C_2	300 W Xemon	Water (72 mL) TEOA (8 mL)	Pt (3 wt.%)	2452	3
PCN/Ti_3C_2	300 W Xemon	Water (45 mL) TEOA (5 mL)	Pt (3 wt.%)	2181	4
PTCN/Ti_3C_2	300 W Xemon	Water (80 mL) MeOH (20 mL)	Pt (2 wt.%)	565	5
g-C_3N_4/V_2C	35 W Xemon	Water (95 mL) MeOH (5 mL)	Pt (3 wt.%)	360	6
Nb_2O_5/g-C_3N_4	300 W Xemon	Water (72 mL) TEOA (8 mL)	Pt (3 wt.%)	6770	7
s-g-C_3N_4/g-C_3N_4	300 W Xemon	Water (90 mL) TEOA (10 mL)	Pt (3 wt.%)	5548	8
Cu/TiO_2@$Ti_3C_2T_x$	300 W Xemon	Water (140 mL) MeOH (10 mL)	---	860	9
Na-g-C_3N_4	300 W Xemon	Water (90 mL) TEOA (10 mL)	Pt (3 wt.%)	143	10
$MnCo_2S_4$/g-C_3N_4	300 W Xemon	Water (80 mL) TEOA (20 mL)	Pt (3 wt.%)	2979	11

Table S8 Calculated PL decay lifetimes from a two-exponential model.

Samples	τ_1 (ns)	τ_2 (ns)	τ_{Avg} (ns)
CN	2.12	10.90	2.32
SCN	1.47	8.35	1.611
SCN/V_2C	1.29	7.37	1.334

Table S9 The fitted time constant from the TAS decay for the samples.

Samples	τ_1 (ps)	τ_2 (ps)
CN	13.30±1.31	456.65±31.87
SCN	6.20±1.25	672.73±119.56
SCNV	10.38±0.26	894.97±11.45

References

[1] Abdul N, Munir A, Ahmad N, et al. Photocatalytic Z-scheme overall water splitting: recent advances in theory and experiments. Advanced Materials, 2021, 33(52): 2105195.

[2] Zuo G, Wang Y, Teo W, et al. Ultrathin ZnIn2S4 nanosheets anchored on $Ti_3C_2T_X$ MXene for photocatalytic H_2 evolution. Angewandte Chemie, 2020, 132(28): 11383-11388.

[3] Wang L, Yang T, Peng L, et al. Dual transfer channels of photo-carriers in 2D/2D/2D sandwich-like $ZnIn_2S_4$/g-C_3N_4/Ti_3C_2 MXene S-scheme/Schottky heterojunction for boosting photocatalytic H_2 evolution. Chinese Journal of Catalysis, 2022, 43(10): 2720-2731.

[4] Xu H, Xia R, Huang J, et al. In situ construction of protonated g-C_3N_4/Ti_3C_2 MXene Schottky heterojunctions for efficient photocatalytic hydrogen production. Chinese Journal of Catalysis, 2021, 42(1): 107-114.

[5] Huang K, Li C, Zhang X, et al. Self-assembly synthesis of phosphorus-doped tubular g-C_3N_4/Ti_3C_2 MXene Schottky junction for boosting photocatalytic hydrogen evolution. Green Energy & Environment, 2023, 8(1): 233-245.

[6] Sherryna A, Tahir M, Zakaria Z. Well-structured V_2C MXenes coupled g-C_3N_4 2D/2D nanohybrids for proficient charge separation with the role of triethanolamine (TEOA) as a protective barrier of g-C_3N_4 for stimulating photocatalytic H_2 production. International Journal of Hydrogen Energy, 2024, 51: 1511-1531.

[7] Dong Q, Chen Z, Zhao B, et al. In situ fabrication of niobium pentoxide/graphitic carbon nitride type-II heterojunctions for enhanced photocatalytic hydrogen evolution reaction. Journal of Colloid and Interface Science, 2022, 608: 1951-1959.

[8] Jiang J, Xiong Z, Wang H, et al. Sulfur-doped g-C_3N_4/g-C_3N_4 isotype step-scheme heterojunction for photocatalytic H_2 evolution. Journal of Materials Science & Technology, 2022, 118: 15-24.

[9] Peng C, Wei P, Li X, et al. High efficiency photocatalytic hydrogen production over ternary Cu/TiO_2@ $Ti_3C_2T_x$ enabled by low-work-function 2D titanium carbide. Nano Energy, 2018, 53: 97-107.

[10] Yi W, Du X, Zhang M, et al. Rational distribution of Ru nanodots on 2D $Ti_{3-x}C_2T_y$/g-C_3N_4 heterostructures for boosted photocatalytic H_2 evolution. Nano Research, 2023, 16(5): 6652-6660.

[11] Zhang L, Ding N, Hashimoto M, et al. Sodium-doped carbon nitride nanotubes for efficient visible light-driven hydrogen production. Nano Research, 2018, 11: 2295-2309.